


Antiferromagnetic ordering and possible lattice response to dynamic uranium valence in U_3O_8 Andrew Miskowicz ^{*}, Tyler Spano , Z. E. Brubaker , and J. L. Niedziela *Nuclear Nonproliferation Division, Oak Ridge National Laboratory, Oak Ridge, Tennessee 37831, USA*D. L. Abernathy *Neutron Scattering Division, Oak Ridge National Laboratory, Oak Ridge, Tennessee 37831, USA*Rodney D. Hunt *Nuclear Energy and Fuel Cycle Division, Oak Ridge National Laboratory, Oak Ridge, Tennessee 37831, USA*S. Finkeldei *Department of Chemistry, University of California Irvine, Irvine, California 92697, USA*

(Received 16 February 2021; revised 1 April 2021; accepted 6 April 2021; published 3 May 2021)

Determining the correct electronic structure of U_3O_8 remains a formidable experimental and theoretical challenge. In the low-temperature phase, two crystallographic U sites are separated into a distinct $2U(V)+1U(VI)$ oxidation configuration. At low temperatures, the U(V) sites form a distorted honeycomb lattice, but the U(VI) sit on a triangular sublattice, suggesting potential for magnetic frustration effects. The spin configuration of the unpaired f electrons on the U(V) sites is likely antiferromagnetic (AFM) from susceptibility measurements, but this has not been confirmed. Here, we present a neutron scattering investigation of the structure and dynamics of U_3O_8 from 1.7 to 600 K. We confirm static AFM ordering onset at between 22 and 25 K, which is present down to at least 1.7 K with AFM peaks corresponding to $[0.5\ 1\ 1]$ and $[0.5\ 2\ 2]$ in the orthorhombic phase. These measurements rule out static AFM order along the a axis of the $Amm2$ phase, a configuration previously suggested by theory. Above 100 K a quasielastic scattering channel opens that we speculate arises from a lattice relaxation response to thermally activated electron hopping. This term does not conform to a magnetic form factor, so it is not related to spin relaxations. If correct, this mechanism stabilizes a continuous valence transition from $2U(V)+1U(VI)$ in the low-temperature ($T < 600$ K) orthorhombic phase to the hexagonal phase that contains only one degenerate U site, wherein the U valence can be dynamically stabilized between $U(V) \leftrightarrow U(VI)$ by phonon-assisted electron hopping.

DOI: [10.1103/PhysRevB.103.205101](https://doi.org/10.1103/PhysRevB.103.205101)**I. INTRODUCTION**

Triuranium octoxide (U_3O_8) is the end product of a number of oxidation pathways for uranium materials in the nuclear fuel cycle, most notably UO_2 . Below ~ 573 K, U_3O_8 (Fig. 1) is orthorhombic ($Amm2$), containing two crystallographic U sites: one U(VI) site and one doubly degenerate U(V) site. Above 573 K, U_3O_8 undergoes a nearly isomorphous structural transition from $Amm2$ to $P\bar{6}2m$ through a slight expansion of the $Amm2$ c axis and contraction of the b axis [1]. The $P\bar{6}2m$ phase has only one crystallographic U site, and the transition from ordered U(V) and U(VI) sites to disordered U valence is speculated to occur, based on heat capacity and electrical conductivity measurements, near 483 K [2]. Thus, there is a region between 483 and 573 K where the U valence is disordered but the structure contains two crystallographically distinct sites.

Temperature-dependent measurements of the structure above 300 K have been the subject of considerable debate [1,3–6]. The precise onset of the structural phase

transition is tightly connected to the oxidation of the material, with less oxidized (i.e., oxygen deficient) U_3O_8 , possessing a *higher* onset temperature of the structural phase transition. Further, formation of the β - U_3O_8 phase appears to affect robust conclusions about thermal expansion behaviors [7,8].

On the other hand, few low-temperature characterizations on U_3O_8 are reported. Particularly notable is the absence of the lattice parameters below room temperature, possibly due to difficulty in handling radioactive materials and preparing stoichiometric specimens of U_3O_8 . Low-temperature magnetic susceptibility measurements have been performed only once, showing a peak in susceptibility at 4.2 K, with two smaller peaks at 8 and 25.3 K, and the 25.3 K corresponds also to a peak in heat capacity [9,10]. No room temperature magnetism is reported [1,11]. General problems with irreproducibility between specimens and across time complicate assessment of magnetic properties [9]. Therefore the magnetic structure of U_3O_8 at low temperatures remains unknown.

In the absence of experimental data, electronic structure calculations such as density functional theory (DFT) have tried to supplement understanding. The complexity of the U_3O_8 system, with two crystallographic sites of mixed oxidation, open $5f$ shell electrons, and a low-symmetry space

^{*}Corresponding author: miskowiczaj@ornl.gov

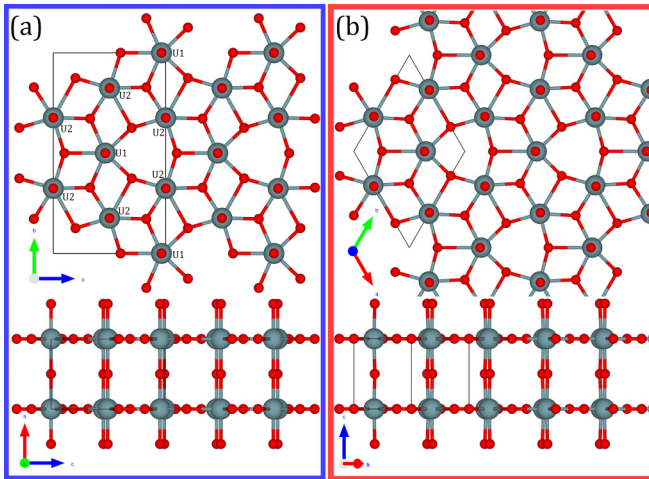


FIG. 1. Structural phases of U_3O_8 . (a) is the low-temperature $Amm2$ phase first described by Loopstra [1]. (b) is the high-temperature hexagonal phase first described by Ackermann [3]. The precise onset of the structural transition is strongly impacted by the synthesis of the U_3O_8 phase, with a higher phase transition temperature apparently induced with a less oxidized sample. Note, in the low-temperature phase (left), the a lattice is out of plane per the original determination, and the b and c lattice constants are in plane. In the high-temperature phase (right), a and b are in plane.

group (relative to the prototypical UO_2), makes it a test system for studying theoretical approaches to actinide oxide modeling [12–17]. A major open question is the relative stability of ferromagnetic (FM) and antiferromagnetic (AFM) configurations. Multiple AFM ordering vectors are plausible in U_3O_8 , and the inclusion of hybrid functionals or spin-orbit corrections (SOC) can affect the free energy significantly.

Because of the fundamental importance of magnetic ordering to the actinide electronic structure community, experimentally measuring the magnetic structure of U_3O_8 is the prime motivator for the present study. A secondary motivator is to investigate the temperature-dependent lattice dynamics through analysis of the phonon density of states (DOS) to determine the relative specific heat contributions that are important for both technological and fundamental purposes.

Neutron scattering is a versatile tool that allows us to access both the structure and dynamic information contemporaneously on a sample as a function of temperature. Here we present analysis of the inelastic neutron scattering (INS) spectra of phase-pure U_3O_8 from 1.7 to 600 K to investigate magnetic ordering and lattice expansion in the elastic channel and to identify magnetic excitations and details of the lattice dynamics in the inelastic channel. This work presents the measurement of both static magnetic ordering in U_3O_8 and its full phonon DOS, and we find a significant interplay of the electronic structure and lattice dynamics.

II. MATERIALS AND METHODS

A. U_3O_8 production

U_3O_8 was formed by calcination of UO_2 (natural isotopic composition) at 973 K for 3 h in air in a Thermolyne 47900 furnace. Details about the calcination procedure are reported

elsewhere [18]. Measurement of the mass gain during calcination indicated a final stoichiometry of $\text{U}_3\text{O}_{7.98}$, corresponding to $\approx 99\%$ oxidation of the initial UO_2 . Precise measurements of the $Amm2 \rightarrow P\bar{6}2m$ structure confirmed the transition temperature to be 578 ± 5 K [19]. A portion of the synthesis precursor was dissolved in nitric acid-deficient uranyl nitrate solution and assessed for impurities with inductively coupled plasma mass spectrometry. The impurity analysis showed that all assayed impurities with magnetic character were present at a level of less than $80 \mu\text{g/g}$ U.

B. Neutron scattering

Time of flight inelastic neutron spectroscopy data were collected on a 10 g powder sample of U_3O_8 using ARCS at the Spallation Neutron Source (SNS, Oak Ridge National Laboratory, Oak Ridge, TN) [20,21]. The sample was enclosed in a 0.5 in. diameter thin-walled Al can and loaded into a top-loading closed-cycle refrigerator. A thin Al foil seal was used between the lid and can body. Data were collected with $E_i = 15, 35, 70,$ and 125 meV, where E_i is the incident neutron energy, with estimated energy resolutions of 0.3, 1.3, 3.8, and 4.4 meV at the elastic line (zero energy transfer), improving to 0.1, 0.4, 0.95, and 1.1 meV at maximal energy transfer for each E_i . An oscillating radial collimator was used to reduce background scattering from the sample environment [22,23]. A background measurement from an empty Al can was measured in identical conditions at all temperatures, and this background was subtracted from the sample data. Measurements were collected at a series of set temperature ranging from 1.7 to 618 K using a pumped helium cryostat for measurements between 1.7 and 100 K, and a closed-cycle refrigerator with a high-temperature stage was used for measurements from 10–618 K. For the closed-cycle refrigerator measurements, a helium exchange gas atmosphere of 100 mbar was used for $T < 300$ K; no exchange gas was used for $T > 300$ K. For temperature-dependent measurements, we discuss correction factors that are applied to the data for measurements above room temperature. Offline *in situ* characterization of the top-loading cryostat showed a temperature-dependent offset of the measured vs set temperature for the system when operated above 300 K. To correct for this, we determined the lattice parameter of aluminum from our empty can measurements, pinned the value of the calculated lattice parameter at 300 K to a standard reference value of 4.0495 Å, and, for the temperatures above 300 K, used the thermal expansion data from Nix to estimate the value of the lattice constant above 300 K. We calculated a polynomial offset to correct the set temperature to the estimated temperature from the lattice constants: $T_{\text{act}} = -46.45 + 1.284T_{\text{set}} - 0.0004T_{\text{set}}^2$ [24]. For the rest of the work, we used the corrected temperature values in referring to experimental results. Data were reduced using Mantid algorithms [25]. All data sets were collected with the same proton charge on the spallation target for consistent normalization. Additional corrections were applied for the detector helium pressure, detector efficiency based on vanadium normalization, and standard masking.

C. Phonon density of states

To calculate the phonon DOS, data are binned into angular regions in 2θ space in 0.25° steps and in energy bins of 1 meV

and then analyzed in the incoherent approximation to obtain the phonon DOS, following a standard procedure [26]. The use of the incoherent approximation is appropriate because of the large number of Brillouin zones probed. The elastic peak was removed, and the data below 3 meV were extrapolated using a Debye model. Data for $S(\mathbf{Q}, \omega)$ were integrated between $4 < |\mathbf{Q}| < 15 \text{ \AA}^{-1}$ and corrected for thermal population. Data from multiple incident energies are combined using the multiphonon package, with a total area weighting scheme [27]. A small, constant, incoherent background is seen in the data and is subtracted from the data during DOS processing.

For single-phonon scattering in a polyatomic material, the inelastic neutron scattering intensity is proportional to the scattering function, which is closely related to the phonon DOS in the case of incoherent scattering:

$$S(|\mathbf{Q}|, \hbar\omega)_{\text{inc}} = \sum_i \sigma_i \frac{\hbar |\mathbf{Q}|^2}{2M_i} \exp(-2W_i) \frac{g_i(\hbar\omega)}{\hbar\omega} [n(T, \hbar\omega) + 1], \quad (1)$$

where σ_i , M_i , and W_i are the neutron scattering cross section, mass, and Debye-Waller factor for atom i , respectively, and $n(T, \hbar\omega)$ is the Bose occupation factor expressed as an explicit function of temperature [28].

The partial phonon DOS g_i is defined as

$$g_i(\hbar\omega) = \sum_j |\mathbf{e}(j, q)|^2 \delta[\hbar\omega - \hbar\omega^p(j, q)], \quad (2)$$

where $\hbar\omega^p(j, q)$ and $\mathbf{e}(j, q)$ are the phonon energies and eigenvectors, which includes information for each phonon branch j and wave vector q [28,29]. As seen from Eq. (1), the measured INS signal provides a neutron-weighted approximation to the true phonon DOS, with the spectral contributions from each species i corresponding to its partial phonon DOS g_i , weighted with $\exp(-2W_i)\sigma_i/M_i$. The Debye-Waller factors for each species are close to unity; however, the ratios of neutron cross section to mass differ substantially: 0.037 for U and 0.2645 for O in units of barns/atomic mass units (amu). The resulting experimental DOS is therefore dominated by contributions from oxygen relative to uranium. The isotopic composition of our sample is natural uranium, thus we use the values for ^{238}U .

To deconvolute the neutron weighting from the experimental DOS we use an estimate of the relative contribution to the DOS of each species at each energy based on density functional perturbation theory (DFPT) calculations. The DFPT calculation provides $g_i(\hbar\omega)$, and by neutron weighting the g_i for each species, a weighting function can be generated to both directly compare the simulations and the data, as well as deconvolute neutron weighting from the measured data:

$$w_f(\hbar\omega) = \frac{\sum_i \frac{\sigma_i}{M_i} g_i^{\text{DFT}}(\hbar\omega)}{\sum_i g_i^{\text{DFT}}(\hbar\omega)}. \quad (3)$$

The instrumental energy resolution as a function of energy transfer is estimated using a parametrization of a Gaussian-convolved Ikeda-Carpenter function and applied to $g_i^{\text{DFT}}(\hbar\omega)$ before calculating $w_f(\hbar\omega)$ [30].

D. Density functional theory

In the discussion below and henceforth in this paper, we refer to the lattice constants in the *Amm2* phase as they appear in Fig. 1; that is, a is the out-of-plane lattice constant and b and c are the in-plane lattice constant. This nomenclature is consistent with the original report [1], but various authors choose a/b in plane, with c out of plane. All references to the literature have been converted to the b/c in-plane and a out-of-plane configuration for consistency.

We briefly review the theoretical electronic structure literature for U_3O_8 . Since U_3O_8 is a semiconductor with unpaired electrons, the Hubbard $+U$ methodology within the DFT framework is appropriate for ground state determinations [12–17]. Without $+U$ to explicitly break the f orbital degeneracy, the ground state is metallic. Using an all-electron full-potential linearized augmented plane wave generalized gradient approximation (GGA $+U$) method, Yun *et al.* found the singly degenerate U(VI) site to be nonmagnetic and the double degenerate U(V) site to have opposite orbital and spin magnetic components, resulting in an FM configuration with $0.41 \mu_B$ per atom aligned along the interlayer c axis, with the FM state 1.5 eV lower than the AFM state, which agrees with Geng *et al.*, who also used a GGA $+U$ approach [13,14]. Later, Brincat *et al.* reported an FM state but remained agnostic on the true ground state, finding “no difference” in total energy among various AFM configurations [17]. In 2013, Wen *et al.* explored in-plane AFM along [001], using both standard GGA $+U$ and the hybrid HSE functional, finding the [001] AFM configuration lower in energy than the FM state [15].

Using GGA $+U$, Ranasinghe *et al.* claim the FM state is 60 meV below the AFM state with the inclusion of SOC, but without SOC the AFM state (along [010], here) was the most stable and in partial agreement with Wen *et al.* who found AFM along [001]. It is not clear why Ranasinghe *et al.* found the [010] AFM configuration to be lower in energy than the [001] configuration using nominally the same level of theory (GGA $+U$) [16].

Nevertheless, a cursory inspection of the crystal structure shows that AFM configurations along [100], [010], [001], [011], or [111] are plausible, and it is clear that this complexity may be a source of discrepancy among literature reports. Another consideration is possible metastable states, convergent electronic states that are not the ground state that arise from the concavity of the $+U$ correction [31]. With the relative energy of various AFM and FM configurations being rather small (<150 meV) this issue must be seriously considered.

With regard to lattice dynamics, only Brincat *et al.* report calculated vibrational entropy of U_3O_8 but comment about the presence of several “imaginary modes,” which may be regarded as an indication of an incorrect electronic ground state [17]. Ranasinghe *et al.* claim the inclusion of SOC may rectify the lattice instability but do not present evidence to this point [16].

To summarize, presently at the GGA $+U$ level of theory, an AFM configuration along either [001] or [010] is believed to be the correct ground state [15,16], with inclusion of SOC stabilizing the FM configuration [16]. The significant literature discrepancies indicate the theoretical determination

of the magnetic configuration in U_3O_8 is neither obvious or straightforward.

In our case, DFT is only used to generate inputs for a weighting function to correct the neutron-weighted phonon DOS $w_f(\omega)$, Eq. (3). Those inputs are the phonon frequencies and eigenvectors, generated using density functional perturbation theory on the $Amm2$ phase using the VASP software package using the GGA-level PBEsol functional [32]. The magnetic structure was assumed to be FM. Given uncertainties in the electronic structure literature, the lattice dynamics calculations on FM U_3O_8 by Brincat *et al.*, the small relative energies between AFM and FM configurations, and the large number of possible AFM configurations (with none corresponding to our own data below), we believe this assumption is appropriate [17]. The initial U_3O_8 structure [1] was relaxed to a final equilibrium geometry with forces < 1 meV/Å. A $2 \times 2 \times 2$ supercell containing 48 U atoms and 128 O atoms was forged for phonon calculations with a $3 \times 3 \times 3$, Γ -centered k -point mesh and 400 eV cutoff energy. Smearing of the partial occupancies was performed with the tetrahedron method with Blöchl corrections with a smearing magnitude of 0.2 eV [33]. The DFT + U method is employed to break f orbital degeneracy, employing the method of Dudarev *et al.*, which uses a spherically averaged $U_{\text{eff}} = \bar{U} - \bar{J}$, where the bar indicates spherical averaging and U and J are the Coulomb and exchange interaction parameters, respectively [34]. We use $U_{\text{eff}} = 2.3$ eV from Beridze *et al.*, who used the linear response approach of Cococcioni and de Gironcoli to calculate U_{eff} for the PBEsol functional for U_3O_8 [35,36]. The partial phonon DOS was generated from the density functional perturbation theory calculations using the Phonopy software package by sampling the Brillouin zone with an $8 \times 8 \times 8$ k -point mesh [37,38].

Small imaginary phonon frequencies were obtained in previous DFT + U calculations [17]. It has been suggested but not shown explicitly that inclusion of SOC could stabilize imaginary phonon modes [16]. We note that SOC adds significant computational expense. Further, although the SOC can alter the ground state geometry and subsequently affect lattice dynamics, our calculations without SOC demonstrate a $2 \times 2 \times 2$ supercell significantly reduces the presence of imaginary modes in the phonon spectrum. For our purposes, the presence of small imaginary modes is of little consequence for calculating the phonon DOS to generate the weighting function, thus we exclude the SOC from our calculations.

Our electron density of states appears extremely similar to the density of states reported by Ranasinghe *et al.*'s GGA + U result, Brincat's GGA + U , and Wen *et al.*'s GGA approach [13,15,17]. Our calculated band gap was 1.55 eV, compared to 1.22, 2.05, and 1.20 eV by those authors, respectively.

III. RESULTS AND DISCUSSION

A. Elastic scattering: Static magnetic ordering

The dynamic structure factor, $S(|\mathbf{Q}|, \hbar\omega)$, collected from INS can be integrated over the momentum or energy transfer, $E = \hbar\omega$, for analysis. This approach allows us to examine individually the static structure, phonon dynamics, and mag-

netic excitations by integrating $S(|\mathbf{Q}|, \hbar\omega)$ over $\hbar\omega$ near 0 energy transfer, over $|\mathbf{Q}|$ in the high $|\mathbf{Q}|$ part of $S(|\mathbf{Q}|, \hbar\omega)$, or examining the low $|\mathbf{Q}|$ part of $S(|\mathbf{Q}|, \hbar\omega)$, respectively.

The INS measurements yield a number of findings. First, we identify previously unconfirmed static AFM order is present for $T < 25$ K. Figure 2, panel (a), shows $S(|\mathbf{Q}|, \hbar\omega)$ for $E_i = 15$ meV integrated over the elastic range, $\hbar\omega = [-0.2, 0.2]$ meV, to filter thermal diffuse scattering from phonons. Static ordering is not present at 40 K; subtracting the 40 K from the 5 K data, residual peaks are fit with Gaussian lineshapes, with resulting fits centered at $Q = 1.314$ and at 2.263 \AA^{-1} [panel (b)]. An additional magnetic peak may be present at $Q = 1.985 \text{ \AA}^{-1}$, but the intensity is quite weak. Looking at potential magnetic ordering configurations, Bragg peak positions of $[0.5 \ 1 \ 1]$ correspond to $|\mathbf{Q}| = 1.311 \text{ \AA}^{-1}$ and $[0.5 \ 2 \ 2]$ to $|\mathbf{Q}| = 2.2733 \text{ \AA}^{-1}$, which reflects a possible AFM propagation vector along the a axis, with a next-neighbor AFM configuration on the U2 sites. AFM propagation strictly along a would produce a magnetic reflection at $\mathbf{Q} = [0.5 \ 0 \ 0]$, corresponding to $|\mathbf{Q}| = 0.76 \text{ \AA}^{-1}$, which is clearly absent from the data shown in Fig. 2. An order parameter measurement obtained by integrating the intensity of the $[0.5 \ 1 \ 1]$ peak as a function of temperature is shown in Fig. 2(c), and from this we extract an ordering temperature of 25 K.

Significant intensity differences are seen between 40 and 5 K near the $[1 \ 0 \ 0]$ Bragg reflection (1.5 \AA^{-1}), reflected in the difference curve in Fig. 2(b). The values of lattice constants extracted from the elastic line fits of the $[1 \ 0 \ 0]$ peak at 5 and 40 K reflect a small increase in the value of the lattice parameter that is consistent across the data set, on the order of 0.01% shift. The residual differences in the $[1 \ 0 \ 0]$ peak can be entirely attributed to this small increase in the a lattice parameter from 5 to 40 K, thus making contribution to the scattering intensity from FM ordering at 5 K implausible.

To aid interpretation of thermodynamic properties, we estimate the lattice constants across the full temperature range. Although the estimated Q resolution is poor compared to a traditional diffractometer, it is possible to quantify the lattice constants by determining the position of Bragg peaks. To do this, the position of the $[1 \ 0 \ 0]$ peak is used to determine the a lattice constant as a function of temperature. The $[1 \ 0 \ 0]$ peak is isolated along the elastic line at 1.51 \AA^{-1} , and the $[2 \ 0 \ 0]$ peak is co-fit with the $[0 \ 6 \ 0]$ and $[0 \ 3 \ 3]$ peaks. The value determined from the refinement is slightly higher by 0.1 \AA for the peak fit obtained from the $[2 \ 0 \ 0]$ peak compared to the $[1 \ 0 \ 0]$ fit. The position of the $[0 \ 0 \ 4]$ was used to determine the c axis constant by fitting a quadruplet of peaks near $Q = 3.7 \text{ \AA}^{-1}$. The $[0 \ 0 \ 4]$ is the strongest contributor to the quadruplet by two orders of magnitude. The $[0 \ 6 \ 0]$ peak is used to report the b -axis parameter, by similarly extracting the peak position by fitting a Gaussian to the triplet of apparent peaks near 3.15 \AA^{-1} and assuming a negligible contribution from the surrounding peaks that are at least two orders of magnitude reduced in intensity from the modeled structure factor. Above 300 K, the $[1 \ 1 \ 0]$ and $[0 \ 0 \ 1]$ peaks of the hexagonal crystal structure description are used to determine the lattice constants. For consistency, the volume of the system as a function of temperature is calculated by conversion of the hexagonal structure to the orthorhombic description. Results for the lattice parameter and volume calculations are shown in

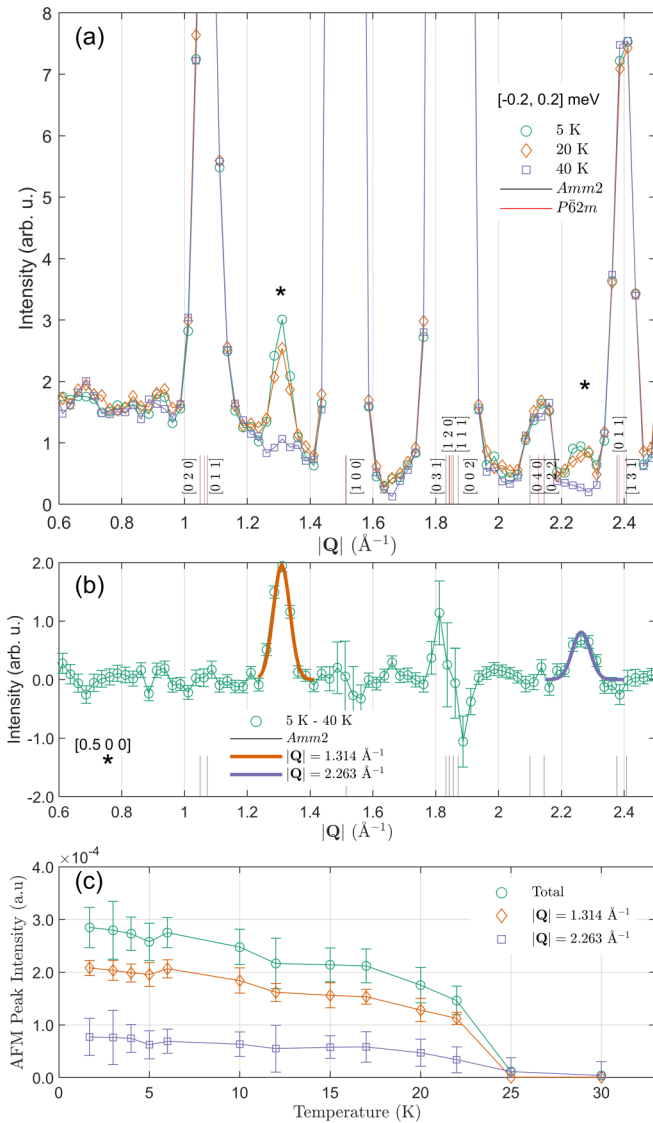


FIG. 2. Analysis of elastic line data showing magnetic structure. (a) Energy filtered $S(\mathbf{Q}, \hbar\omega)$ obtained by integrating over the range $\hbar\omega = [-0.2, 0.2]$ meV for $E_i = 15$ meV data. Black, blue, and red curves show data for 5, 20, and 40 K, respectively. The presence of peaks in the 5 and 20 K data due to static AFM order are indicated with asterisks. The phase location indicators for the orthorhombic phase from Loopstra [1] and the hexagonal phase from Ackermann *et al.* [3] are shown in black and red, respectively. (b) Difference curve obtained from subtracting 40 from 5 K data. Shifts in Bragg peaks are explainable through thermal expansion—no additional intensity from FM ordering is detected. The presence of two unsubtracted peaks near $|\mathbf{Q}| = 1.314$ and 2.263 \AA^{-1} could correspond to Bragg positions $[0.5 \ 1 \ 1]$ and $[0.5 \ 2 \ 2]$ of the nuclear cell, suggesting a complex AFM arrangement. No magnetic peaks are observed at $[0.5 \ 0 \ 0]$, ruling out static order along the a axis of the $Amm2$ phase. (c) Intensity of the magnetic peaks at $|\mathbf{Q}| = 1.314$ and 2.263 \AA^{-1} and their sum as a function of temperature, showing a transition to the ordered state occurring between 20 and 25 K.

Fig. 3 and tabulated in Table I. Error bars on lattice parameters are carried over from the uncertainty in the $|\mathbf{Q}|$ position resulting from the fit and similarly for the volume estimation. The unit cell volume uniformly decreases with temperature

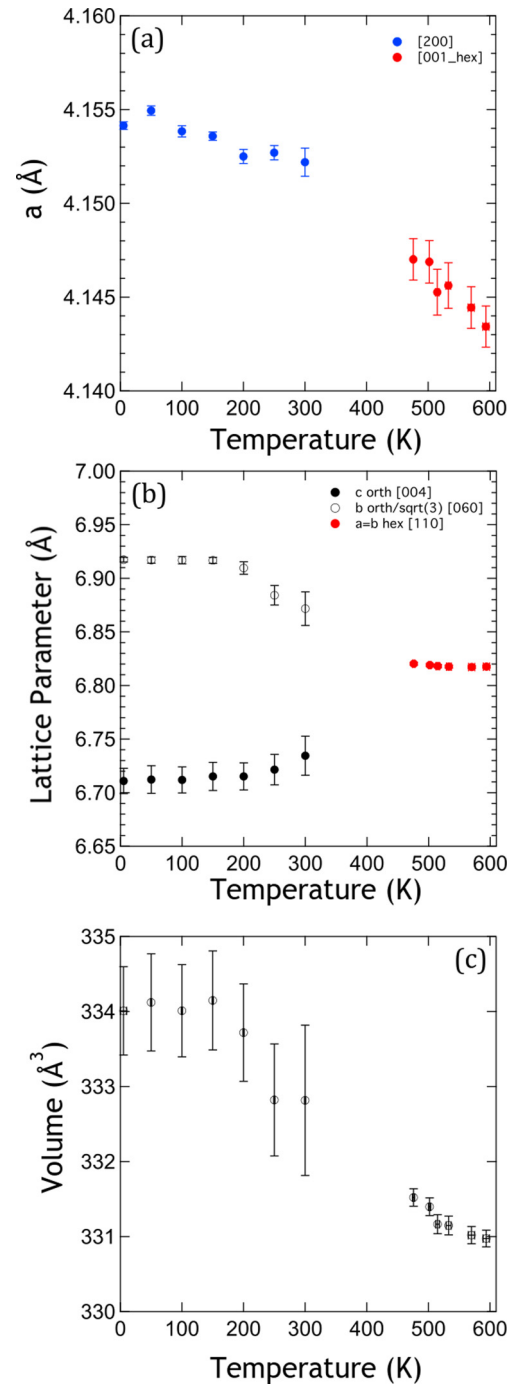


FIG. 3. Lattice constants of U_3O_8 as a function of temperature. In panel (a), the out-of-plane (orthorhombic) a and (hexagonal) c lattice constants as determined from the $[200]$ Bragg peak position below 300 K and from the $[001]$ peak above 300 K. (b), in-plane orthorhombic b/c lattice constants from the $[004]$ and $[060]$ Bragg peaks and degenerate hexagonal $a = b$ lattice constant determined from the hexagonal $[110]$ peak. (c) Volume of unit cell calculated in the orthorhombic configuration across the full temperature range. The temperature dependence shows that the known decrease of a , b , and the unit cell volume above 300 K originates essentially at 0 K.

starting at 1.7 K. Error bars on the temperature scale reflect the uncertainty from our temperature correction procedure. The anisotropic lattice expansion of U_3O_8 above room temperature

TABLE I. Lattice constants of α - U_3O_8 at 5 K.

| T K | Ref. | a Å | b Å | c Å | Vol. Å ³ |
|--------|---------------|----------|----------|----------|------------------------|
| 5 | This work | 4.15(4) | 11.9(8) | 6.7(2) | 33(4) |
| 300 | This work | 4.15(2) | 11.9(7) | 6.7(3) | 33(3) |
| 296 | Ackermann [3] | 4.149 | 11.961 | 6.726 | 333.785 |

has been reported [3,19]. However, because no lattice parameters of U_3O_8 below 300 K have been reported, we present all calculated lattice parameters for qualitative information. Despite the large uncertainty, the temperature dependence of the lattice constants in Fig. 3 shows that the trend of the a and b lattice constants is to *decrease* with increasing temperature below 300 K, although c is increasing. The decrease in a and b lattice constants matches the known high-temperature (300+ K) behavior of U_3O_8 [3], but the uniform decrease of the total volume of the system with increasing temperature from 5 K, shown in Fig. 3(c), has not been previously reported. As the lattice constants are highly dependent on precise sample stoichiometry, we use the extracted values for analysis of the heat capacity presented later.

B. Inelastic scattering: Magnetic excitations

We now look at the magnetic excitation spectrum of U_3O_8 . Figure 4 shows $S(|\mathbf{Q}|, \hbar\omega)$ at 5 K [panel (a)] and 25 K [panel (b)] for $E_i = 15$ meV. The most prominent features in $S(|\mathbf{Q}|, \hbar\omega)$ are two strong peaks at 5.5 and 6.8 meV. These excitations persist up to 22 K with decreasing intensity with increasing temperature. Above 25 K, intensity associated with these excitations collapses, shown explicitly though integrating intensity along E in Fig. 4(c). Panel (c) shows the dynamic susceptibility, $\chi''(|\mathbf{Q}|, \hbar\omega) = (1 - \exp(-\hbar\omega/k_B T))S(|\mathbf{Q}|, \hbar\omega)$, which removes the temperature dependence of phonon scattering, allowing comparison across temperatures. Magnetic scattering is present above 22 K, but its excitation spectrum is broader with no sharp peaks and is clearly different in character. A significant amount of scattering is also present below 4 meV. These features also decrease in intensity with increasing temperature, although a phase transition at 22 K is less apparent as the broadening of the elastic line is relevant out to 1.7 meV at 22 K.

The magnetic form factor, $F(Q)$, presented in panel (d) for the peak centered at 5.5 meV, shows a gradual decrease in intensity in the lower $|\mathbf{Q}|$ regions up to 22 K, at which point the same phase transition detected in Fig. 2 is observed. The theoretical form factor for a free f electron appears to be approximately valid. In the AFM ordered state individual electrons are localized to the U(V) ions and experience a crystal field interaction with the O ligands, which form a distorted pentagonal bipyramidal coordination environment. It is possible that the well-defined excitations at 5.5 and 6.8 meV, as well as the apparent excitations below 4 meV, result from the low symmetry crystal field potential. Above 22 K, the AFM order is lost, and the sharp excitation peaks are lost. If the peaks are related to a crystal field interaction, their disappearance indicates that the underlying ligand field itself has changed, the U(V) electrons are no longer localized, or the

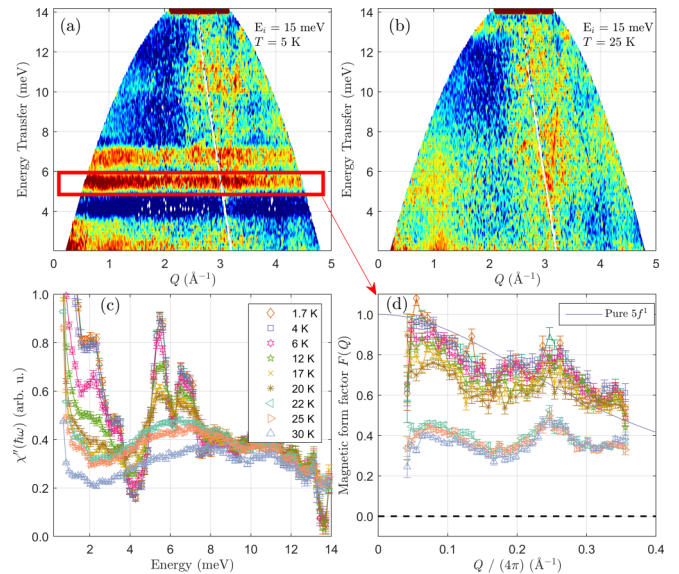


FIG. 4. Dynamic structure factor $S(|\mathbf{Q}|, \hbar\omega)$ of U_3O_8 at 5 K [panel (a)] and 25 K [panel (b)] measured with $E_i = 15$ meV. Two magnetic excitations are observable near 5.5 and 6.8 meV, with a significant reduction in intensity observed at 22 K. (c) $\chi''(|\mathbf{Q}|, \hbar\omega)$ for U_3O_8 integrated over all $|\mathbf{Q}|$ between 1.7 and 30 K. $\chi''(|\mathbf{Q}|, \hbar\omega)$ shows these magnetic excitations decreasing in intensity and transitioning to a distinct state at 22 K, commensurate with the loss of AFM order. Substantial additional magnetic structure is observed below 4 meV, which also undergoes a decrease in intensity in this temperature range. (d) Magnetic form factor $F(Q)$ for U_3O_8 [same temperature legend as (c)] integrated over the energy range $E = [4.8, 6]$ meV and normalized to the maximum value for the 1.7 K data set, showing a decrease in magnetic intensity especially in the low $|\mathbf{Q}|$ region. The theoretical magnetic form factors for U(V) (f^1) are also shown. For U, f^1 , f^2 , and f^3 are nearly identical in this $|\mathbf{Q}|$ range. The abrupt change between 20 and 25 K is also observed in the $|\mathbf{Q}|$ dependence of the form factor, with a sharp decrease in intensity, especially below $4\pi \cdot 0.2 \text{ \AA}^{-1}$. Visually, the difference in form factor between 5 and 25 K appears to be a comparable shape to the form factor for f^1 , which may be expected for magnetic crystal field excitations.

strength of the crystal field interaction relative to some other interaction becomes small. One possible explanation would be a structural distortion induced by the thermal occupation of the very low energy (< 2 meV) magnetic states.

It is possible that the magnetic excitation spectrum reflects gapped spin wave excitations of the magnetic order. The existence of multiple spin waves would be permitted in an Ising interpretation, with inclusion of requisite anisotropy. In this case, above the ordering temperature, the static structure at $|\mathbf{Q}| = 1.314 \text{ \AA}^{-1}$ would represent remnant short ranged magnetic order. However, the extended $|\mathbf{Q}|$ range of the magnetic excitations at 6.8 and 5.5 meV, and to a lesser extent visible near 2 meV, for $T < 22$ K point to a highly localized spin excitation, and is not commensurate with a spin wave.

C. Inelastic scattering: Phonons

We next examine the temperature-dependent behavior of the phonons. First, $S(\hbar\omega)$ is formed by integrating $S(|\mathbf{Q}|, \hbar\omega)$

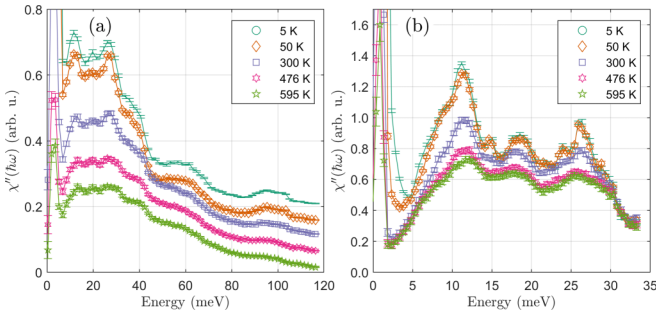


FIG. 5. $\chi''(|\mathbf{Q}|, \hbar\omega) = (1 - \exp(-\hbar\omega/k_B T))S(|\mathbf{Q}|, \hbar\omega)$ shown for (a) 125 meV integrated over $|\mathbf{Q}| = [4, 15] \text{ \AA}^{-1}$. Data are offset by 0.05 per data set for presentation. A notable increase in phonon mode width is observed for 300 K and above for oxygen modes. (b) 35 meV, integrated over $|\mathbf{Q}| = [4, 7] \text{ \AA}^{-1}$. These data, not offset, show a substantial decrease in intensity up to 595 K.

over $|\mathbf{Q}|$ from 4 to 12 \AA^{-1} for the $E_i = 125$ meV data. The resulting $S(\hbar\omega)$, and related dynamical susceptibility, $\chi''(\hbar\omega) = (1 - \exp(-\hbar\omega/k_B T))S(\hbar\omega)$, are shown in Fig. 5.

The dynamic susceptibility includes a temperature term such that χ'' can be compared at different temperatures, as before. A general decrease in intensity and broadening of modes is seen in these plots. Particularly notable is the loss of coherence of the modes above 80 meV, attributed to oxygen from our calculations and general physical intuition.

The decrease in intensity for $\chi''(|\mathbf{Q}|, \hbar\omega)$ is unusual. In the harmonic approximation for lattice dynamics, the integral of the phonon scattering intensity corrected for thermal population effects should be conserved and proportional to the sample mass. The lattice changes are quite slight across the full measured range, suggesting that the harmonic approximation should be approximately valid, yet there is a pronounced alteration to the observed phonon modes and the odd intensity dependence. A few resolutions to this are credible. The first possible explanation for the intensity nonconservation is the presence of magnetic scattering above 4 \AA^{-1} , persisting up to 300 K. As the magnetic form factor decreases rapidly with increasing $|\mathbf{Q}|$, we generated $\chi''(|\mathbf{Q}|, \hbar\omega)$ with a variety of low momentum transfer cutoffs up to 10 \AA^{-1} . The intensity nonconservation remains for all momentum transfer cutoffs, indicating that a magnetic component of $\chi''(|\mathbf{Q}|, \hbar\omega)$ was

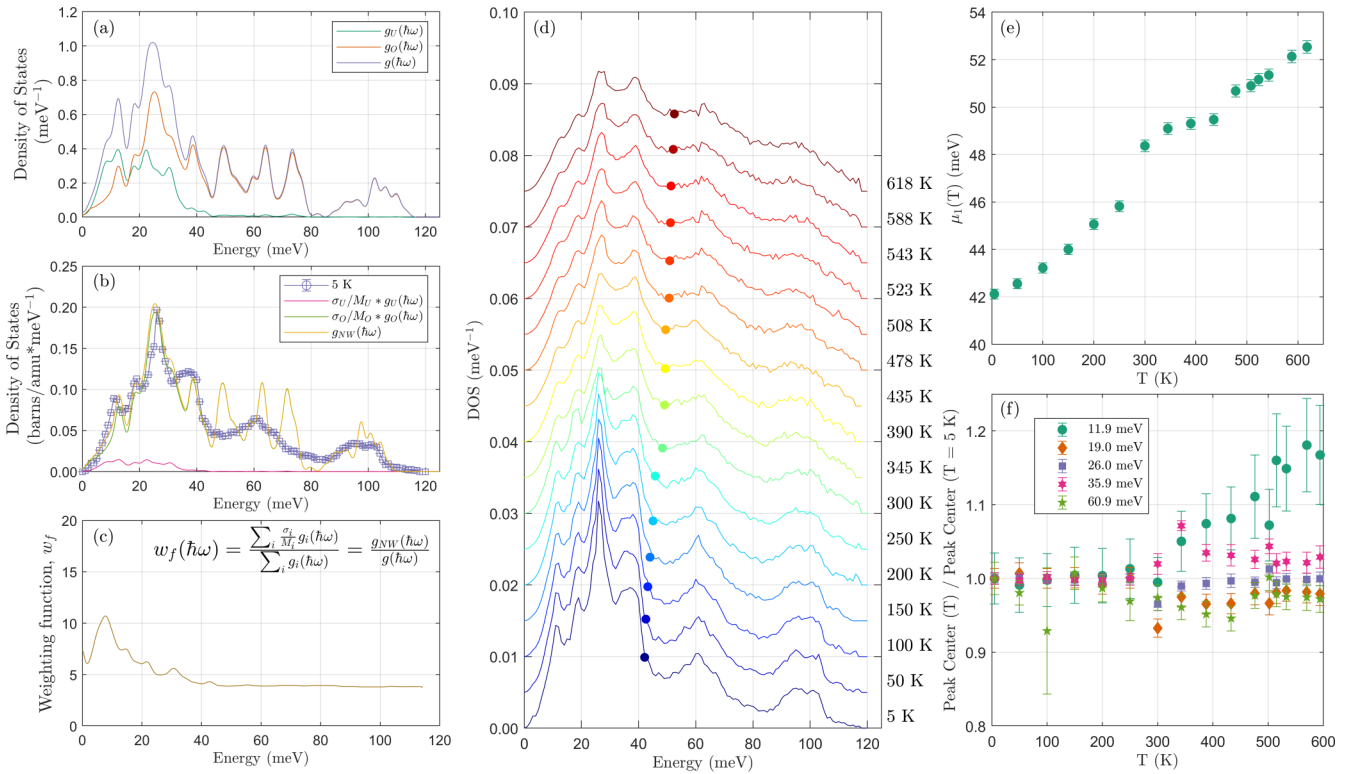


FIG. 6. (a) Atom projected DOS from DFT. The energy scale of the DFT data has been expanded by 5% to match the phonon cutoff between the experiment and DFT data. (b) Stitched, deweighted DOS data at 5 K and same DFT data as (a) but accounting for neutron weight. (c) The weighting function, the quotient of the total ($g_U + g_O$) unweighted phonon DOS, and the neutron-weighted DOS designed to correct for the neutron's relative sensitivity to the O atoms in the INS measurement. (d) The combined, deweighted phonon DOS as a function of energy transfer and shown with increasing temperature across the full measured temperature range. The filled points are positioned in energy at the value of the first moment of the phonon DOS for each temperature and are plotted independently in panel (e). The first moment of the phonon DOS shows a quadratic trend to 300 K and a shift to a linear trend at 476 K and above. (f) The result of Gaussian fitting to peak positions in the phonon DOS for $E < 62$ meV, normalized to the values at 5 K. The lowest energy mode in the phonon DOS exhibits a sharp increase in mean energy when normalized to the low-temperature value; the rest of the modes remain relatively constant or slightly decrease consistent with thermal expansion behaviors. Modes attributed to high energy oxygen modes become challenging to quantify above 300 K because of the general smearing of the DOS information.

not significant. A more credible scenario is that the decrease in $\chi''(|\mathbf{Q}|, \hbar\omega)$ with temperature is strong evidence for the presence of significant electron-phonon coupling in U_3O_8 .

The phonon DOS is necessary to determine the vibrational entropy S_{vib} , which is typically the largest contributor to the heat capacity of a semiconductor at finite temperature, and it is the building block of understanding anharmonicity in lattice dynamics and thermal transport [39]. Figure 6(a) shows the neutron weighted and atom projected DOS contributions for O and U as calculated with DFT, along with the total and direct comparison to the experimentally measured DOS data at 5 K in panel (b). This figure indicates that the phonon DOS is primarily U motion below 20 meV and O motion above 20 meV. Generally, good agreement is found between the theoretical DOS and the measured DOS; in particular, the calculation captures the strongest phonon feature at 25 meV.

Figure 6(c) shows the weighting function $w_f(\hbar\omega)$ convolved with the estimated instrumental energy resolution across the measured ranges, accounting for the different energy resolutions of the incident energies used in the experiment. The weighting function increases the observed $S(|\mathbf{Q}|, \hbar\omega)$ below 20 meV where the majority of the phonon DOS is from U motion and is smaller and flat above 20 meV wherein the motion originates from O atoms, representing the relatively weaker neutron-phonon interaction with U. Figure 6(c) emphasizes the importance of having an estimate of the theoretical phonon DOS from calculations because the magnitude of the weighting function's energy dependence is large in this case because of the large difference in mass between U and O.

The phonon DOS are extracted from the combined $S(|\mathbf{Q}|, \hbar\omega)$ data from $E_i = 35, 70,$ and 125 meV measurements and are deweighted to correct for the disparity in cross section as described earlier. These corrected data are shown as a function of temperature in Fig. 6(d). With increasing temperature, the phonon DOS broadens, most notably in the higher energy, O-motion regions.

The first moment of the DOS is given by

$$\mu_1(T) = \frac{\sum_{\hbar\omega} g(\hbar\omega)\hbar\omega}{\sum_{\hbar\omega} \hbar\omega} \quad (4)$$

and is shown in Fig. 6(e). As illustrated in the figure, the first moment of the deweighted DOS uniformly *increases* and is additional evidence for electron phonon coupling. Plotting the first moment against the volume, the frequency is negatively correlated with unit cell volume with a slope of $-2.96 \text{ meV}/\text{\AA}^3$.

The main phonon features appear at 6.9, 11.6, 18.1, 23.8, 26.1, and 28.2 meV with smaller features at 14.7 and 21.9 meV. With higher incident energy, the phonon features are well described by a series of peaks centered at 35.7, 54.0, and 96.0 meV.

To assess the relative shifts in phonon behavior as a function of temperature, we fit bands of intensity in the phonon DOS for $E < 60$ meV from the stitched data, and results are shown in Fig. 6(f), normalized to the value at 5 K. The center position of the lowest energy peak near 11 meV at 5 K shows a striking increase in position, and the remaining peaks exhibit a decreasing or static trend. Bands of modes at higher energies

become too indistinct with increased temperature to resolve shifts. Because the phonon DOS at 11.9 meV is primarily U motion, this shift indicates a hardening of phonon interactions with increasing temperature. A possible explanation for this behavior involves the increase in long-range magnetic interaction strength between U atoms, which is mediated by the decrease in unit cell volume. The structural phase transition in U_3O_8 to $P\bar{6}2m$ occurs at 573 K and has only one U site. Thus, the electronic configuration must become disordered at or below 573 K, and it is possible that an increase in electron mobility affects an increase in U-O and U-U screening, reflected in the hardening of the phonon DOS in the 11.9 meV band.

D. Adiabatic charge transfer and quasielastic lattice response

Two pieces of evidence suggest that an additional scattering component is present in the inelastic data. First, the nonconservation of $\int \chi''(\omega, T)d\omega$ requires the existence of an additional contribution to χ'' at elevated temperatures. Because the total neutron scattering cross section is conserved, an increasingly larger fraction of the total scattering intensity must come from this additional contribution, and this is reflected in the decreasing temperature dependence of $\int \chi''(\omega, T)d\omega$. We eliminated the possibility of magnetic contributions by noting that the nonconservation is independent of the $|\mathbf{Q}|$ integration range. Second, in Fig. 6(f) the lowest energy peak position increases with temperature, a rather unusual behavior that suggests an additional low energy scattering component could be interfering. Therefore, the hypothetical additional scattering component could take a phononlike $|\mathbf{Q}|$ dependence and could be centered near or at zero energy transfer.

In fact, there is an additional scattering component that appears as a quasielastic (QENS) term. Its functional form is given by a Lorentzian component, centered at zero energy transfer, whose width and intensity increase with temperature. We apply a scattering law with the following form for $S(\hbar\omega, T)$:

$$S(\hbar\omega, T) = A(T)\delta(\hbar\omega) + L(T)\frac{1}{2\pi} \frac{\Gamma(T)}{(\hbar\omega - \hbar\omega_0)^2 + \frac{1}{4}\Gamma(T)^2}, \quad (5)$$

where $A(T)$ and $L(T)$ are the elastic and QENS intensities and $\Gamma(T)$ is the quasielastic full width at half maximum. The scattering law is convoluted with a resolution function composed of the collected spectrum at 1.7 K, which allows us to faithfully include the phonon contribution in the elastic term. Although the 1.7 K spectrum contains the crystal field excitations that disappear near 22 K, this spectrum seemed appropriate to model the phonon scattering at all temperatures because the QENS term is broadband and fairly insensitive to the details of phonon excitations.

In Fig. 7, we plot several examples of this QENS feature and the resultant Lorentzian parameters. We now clearly see that the increase in QENS intensity with width on the order of 10–20 meV explains the hardening of the phonon feature in Fig. 6(f); in fact, this shift in position is due to the presence of an underlying incoherent feature. Moreover, the intensity of this term is significant compared to the delta function (phonon) term, which explains the nonconservation of χ'' .

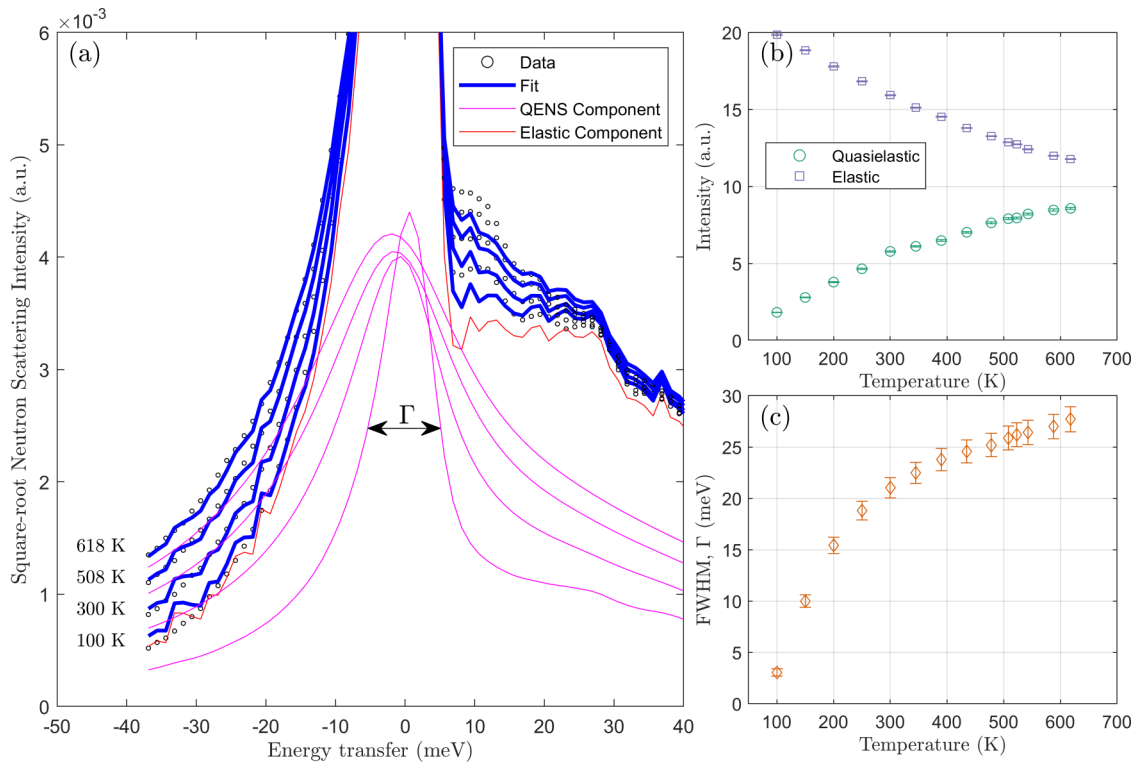


FIG. 7. (a) Example quasielastic spectrum at 100, 300, 508, and 618 K, including a Lorentzian component and a δ function centered at zero energy transfer. Both components are convolved with a resolution function, which is taken from the phonon spectrum at 2 K. Using the low-temperature spectrum allows us to faithfully reproduce phonon features. Below 100 K, no significant quasielastic term can be discerned. $S(\hbar\omega)$ is formed by integrating over all $|\mathbf{Q}|$ for this analysis. (b) QENS intensity as a function of temperature, showing a nearly monotonic increase, with a change in slope near 350 K. (c) Quasielastic full width at half maximum (Γ) as a function of temperature, showing a monotonic increase.

We hypothesize that the QENS component originates from the relaxation of ions responding to the adiabatic transfer of electrons between U sites, resulting in $5f^0 \longleftrightarrow 5f^1$ [$\text{U(VI)} \longleftrightarrow \text{U(V)}$]. Such “intermediate-valence” systems are common in rare earth compounds, which have a dynamical mechanism for transitions between, typically, RE^{+3} and RE^{+2} states of a specific ion [40]. In those rare earth systems, the time-averaged valence configuration is therefore neither 2 nor 3, but an intermediate value with an adiabatic valence fluctuation timescale that is small compared to the ionic relaxation timescale. An intermediate-valence system must be distinguished from a mixed-valence system, in which multiple metal sites sustain distinct oxidation configurations. Strictly speaking, U_3O_8 is a mixed-valence state *below* 573 K and an intermediate-valence system *above* 573 K. However, the U sites are nearly structurally degenerate below 573 K, so it is reasonable that the energetic difference between $5f^0$ and $5f^1$ are small and that a hypothetical electron hopping mechanism between sites should be thermally accessible. In fact, a mechanism for balancing the charges between U sites *must* be thermally accessible because it is required to manifest the high-temperature $P\bar{6}2m$ phase at 573 K. Depending on the temperature, U_3O_8 behaves like either an intermediate-valence system (high temperature) or a mixed valence system (low temperature), with the structural phase transition reflecting the *ionic* response to both of these configurations.

Our physical model involves the hopping of electrons from U(V) sites to U(VI) sites at a temperature-dependent frequency. At all temperatures, it is reasonable to assume the electron hopping timescale is much faster than the ionic relaxation timescale, but above 573 K, the hopping rate is large enough that the ions respond to an *effective* charge configuration of U(16/3), which results in a strict structural degeneracy. Below 573 K, the hopping rate is slow enough that distinct U(V) and U(VI) sites still exist, but there is a component of ionic motion related to ions responding to the new charge configuration. The width and intensity of this ionic relaxation increases with temperature due to the increase in the electron hopping rate—at low temperatures, the electron hopping is rare so the intensity of the relaxation is muted, whereas near the transition it is much more significant.

The ionic relaxation must occur in a QENS channel and not an inelastic channel. If the ionic relaxation appeared at finite energy transfer, it would imply that the phonon dynamical matrix contained additional nonzero eigenvalues, which is not possible without modifying the lattice symmetry.

Quasielastic *magnetic* excitations have been observed in the mixed-valence $\text{Sm}_{0.66}\text{Y}_{0.33}\text{S}$, which are the result of the presence of a many-body singlet ground state (as opposed to a single-ion singlet ground state) [41]. Similarly, in cerium-lanthanum-thorium alloys quasielastic scattering is present and centered either at zero or at finite energy transfer and has been explained by spin-relaxation dynamics either in

noncrystal field effect ions (zero energy transfer) or crystal-field ions (finite energy transfer) [42–44]. In addition to the $|\mathbf{Q}|$ -averaged data, we investigated the $|\mathbf{Q}|$ -dependent part of the quasielastic scattering at several prototypical temperatures (details not shown). Instead of decreasing with increasing $|\mathbf{Q}|$, as would be expected with a magnetic excitation, the quasielastic intensity peaks around 12 \AA^{-1} and is slightly decreasing above, commensurate with a phononlike form factor. The $|\mathbf{Q}|$ dependence of the quasielastic width is $|\mathbf{Q}|$ independent, which is expected behavior for QENS at very high $|\mathbf{Q}|$. This form factor eliminates a magnetic origin of the QENS feature.

Thermally activated electrons imply the existence of valence disorder in U_3O_8 at all temperatures. Recently, we showed that the high-temperature ($\geq 600 \text{ K}$) U_3O_8 structure, which has only one crystallographic U site, does not exhibit long-range charge ordering, eliminating the possibility of a subtle superlattice configuration [19]. Here, we show that the oxidation configuration could be stabilized by the dynamic coupling of valence fluctuations between U sites to lattice phonons.

E. Heat capacity

We now use the experimental results to assess heat capacity contributions. The vibrational entropy S_{vib} may be determined from the relation [39]:

$$S_{\text{vib}} = 3Nk_B \int_0^\infty g_m(\hbar\omega, T) [(1 + n_T) \ln(1 + n_T) - n_T \ln(n_T)] d(\hbar\omega), \quad (6)$$

where N is the number of atoms in the crystal and $g_m(\hbar\omega, T)$ is the contribution of the deweighted phonon DOS for temperature T . The estimated S_{vib} extracted from the deweighted experimental phonon DOS is shown in Fig. 8.

The total heat capacity of a solid can be expressed as the sum of distinct components [45]:

$$C_p \approx C_v + C_D = C_D + C_{VH} + C_{VA} + C_{e^-} + C_M + C_{VV}, \quad (7)$$

where C_p and C_v are the constant pressure and constant volume heat capacities; C_D is the dilatational correction found from $C_p - C_v$, C_{VH} and C_{VA} the harmonic and anharmonic vibrational contributions, C_{e^-} is the contribution from conduction electrons, C_M the contribution from spin states (crystal field excitations and magnetic excitations), and C_{VV} the contribution from lattice vacancies.

The total vibrational heat capacity of U_3O_8 can be calculated from the measured neutron deweighted experimental phonon DOS $g_m(\hbar\omega, T)$ at temperature T using

$$C_p(T) = \sum_i g_m(\hbar\omega_i, T) k_B \left(\frac{\hbar\omega_i}{k_B T} \right) \frac{\exp(\hbar\omega_i/k_B T)}{[\exp(\hbar\omega_i/k_B T) - 1]^2}, \quad (8)$$

where the sum occurs over all energy bins. As noted previously, this total heat capacity C_p is a sum of the harmonic heat capacity C_{VH} and a number of smaller terms. C_{VH} can be calculated from experimental phonon DOS by using constant phonon DOS at 5 K [i.e., $g_m(\hbar\omega, T = 5 \text{ K})$] for all temperatures in Eq. (8). The estimation of the total vibrational

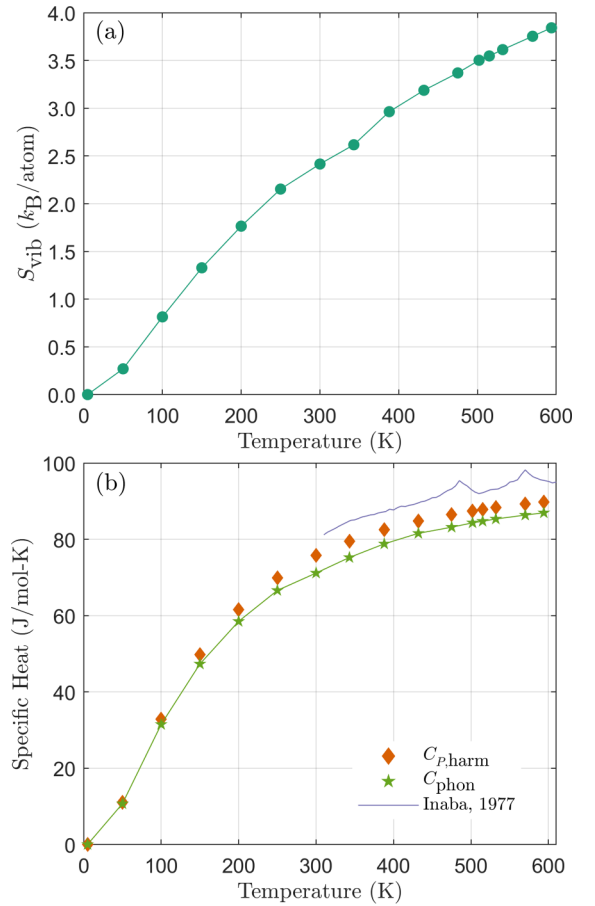


FIG. 8. (a) Vibrational entropy of U_3O_8 calculated from deweighted neutron DOS from Eq. (6). (b) C_p of U_3O_8 extrapolated value of the harmonic contribution estimated from data at $T = 5 \text{ K}$ ($C_{p,\text{harm}}$) and calculated from the deweighted neutron DOS from Eq. (8) (C_{phon}) compared with values from literature [2]. The value of the estimated harmonic contribution is higher for all $T > 5 \text{ K}$.

contribution obtained from the deweighted, stitched experimental DOS is presented in Fig. 8 with the estimated harmonic component and compared with available experimental data from the literature [2]. As the figure shows, the value of the extracted vibrational component underestimates the value of the experimental data by about 11%, except for the areas containing λ anomalies. Also, the figure shows that the value of the harmonic contribution is overestimated across the whole range over the estimated lattice contribution. This observation is not surprising given the observation of negative thermal expansion across the full range of data and the commensurate shift to higher energy of the first moment of the DOS.

Considering the other terms in Eq. (7), the C_D is given by:

$$C_D = \frac{\alpha(T)^2 V(T) T}{\chi(T)}, \quad (9)$$

where $\alpha(T)$ is the volumetric thermal expansion coefficient, $V(T)$ is the volume, and $\chi(T)$ is the compressibility (inverse of bulk modulus) at temperature T . From the total and dilatational heat capacity, the volumetric heat capacity C_v can be calculated using

$$C_v = C_p - C_D. \quad (10)$$

To calculate the dilatational component of the specific heat, we use values of the lattice thermal expansion coefficients and volumetric expansion from the present work. The lattice thermal expansion coefficients are fit in three separate ranges to create a piecewise linear function of the expansion coefficients, and the volumetric expansion is calculated by converting the hexagonal lattice parameters to the orthorhombic setting for consistent volume comparison across the range. The value of the bulk modulus from the computational work of Brincat on the polymorphs of U_3O_8 was used to estimate the compressibility, again using a piecewise linear function at the different operating ranges (values used included 165 and 181 GPa for the orthorhombic and hexagonal phases) [17]. As might be expected from the relatively small change of the volume over the range (decrease in total by 0.1% from 5–594 K) and the relatively large value of the bulk modulus, the C_D is effectively negligible.

Thus we arrive at the condition that the disparity between the experimentally measured C_p has a significant contribution from one of the additional terms available. First, as U_3O_8 is a semiconductor at all temperatures, we assume negligible contribution from the conduction electrons. Next, the contribution from spin states, C_M , is complex to evaluate. The static AFM structure and resultant spectrum of magnetic excitations observed from 1.7 to 300 K in this report indicate there is likely some role for spin contribution to the total specific heat. However, absence of static magnetic order in our measurements from 22 K and above makes this difficult to assess as there are no known relationships to calculate contributions to heat capacity from short ranged magnetic order in semiconductors; further, this is unlikely to be an issue in the hexagonal phase. C_{VV} , the contribution from lattice vacancies, is a candidate for additional contributions to the heat capacity because of the historic difficulty in precisely controlling the stoichiometry of U_3O_8 compounds, but no estimation is available for the location of vacancies within the lattice, nor are numbers available for vacancy formation. Thus, we conclude that at least some of the distinctions in heat capacity are due to vacancy and anharmonic contributions, but they require further investigation and larger scale computational simulations than are currently accessible.

Finally, we must acknowledge that the presence of the incoherent quasielastic term affects C_p because some of the neutron scattering power that would normally be conserved in $g_m(\hbar\omega, T)$ instead comes in the incoherent Lorentzian term. What is occurring is a transfer of scattering power from $S(\hbar\omega)$ toward a lower energy part of the spectrum. $g_m(\hbar\omega)$, proportional to $S(\hbar\omega)\hbar\omega$, is therefore weighted to lower energy due to this effect. It is not obvious to what degree this scattering power transfer affects C_{phon} , but its contribution to $g_m(\hbar\omega)$ is non-negligible. In addition, the quasielastic term is symmetric across zero energy transfer, so some of the scattering power is lost to the negative energy transfer channel, further reducing $g_m(\hbar\omega)$.

IV. CONCLUSIONS

We present evidence of previously unconfirmed static AFM order in stoichiometric U_3O_8 at low temperature,

accompanied by a complex spectrum of magnetic excitations. No magnetic Bragg peak intensity is observed along $[0.5\ 0\ 0]$, which contradicts recent DFT calculations of U_3O_8 [15]. Magnetic excitations are present at 5.5 and 6.8 meV, as well as additional complex magnetic scattering below 4 meV, which we attribute to excitations of the pentagonal bipyramidal U(V) crystal field potential. A magnetic phase transition occurs from AFM to non-AFM at between 22 and 25 K, at which temperature the magnetic peaks disappear, and the crystal field is destabilized and the intensity associated with these excitations collapses. Below 22 K, the magnetic form factor indicates that the excitations are primarily localized, conforming to the expected form factor for isolated f^1 species. Above 22 K, some delocalization of the magnetic excitation is observed.

Above 100 K, an incoherent, quasielastic scattering term appears. Its intensity and full width at half maximum are monotonically increasing with temperature, approaching 25–30 meV at 600 K. Possible magnetic origin of this term is eliminated due to the $|\mathbf{Q}|$ dependence of the scattering, conforming instead to a phononic form factor. We hypothesize that this term represents the incoherent relaxation of ions to transient changes in U oxidation state, affected by the hopping of electrons between U(V) to U(VI) sites. The rate of this electron hopping interaction is slow enough to support distinct U oxidation states below 600 K, but the hexagonal phase represents a true fluctuating valence state and the electron hopping is adiabatic. The presence of the incoherent scattering term indicates that instability in the U oxidation state occurs at temperatures as low as 100 K. U_3O_8 is a mixed oxidation state system at low temperature and an intermediate valence system above 600 K and the structural phase transition can be considered a reflection of this distinction.

The Department of Energy will provide public access to these results of federally sponsored research in accordance with the DOE Public Access Plan [46].

ACKNOWLEDGMENTS

A portion of this research used resources Spallation Neutron Source, a DOE Office of Science User Facility operated by the Oak Ridge National Laboratory. This research used resources of the Compute and Data Environment for Science (CADES) at the Oak Ridge National Laboratory, which is supported by the Office of Science of the U.S. Department of Energy under Contract No. DE-AC05-00OR22725. This manuscript has been authored by UT-Battelle, LLC under Contract No. DE-AC05-00OR22725 with the U.S. Department of Energy. The United States Government retains and the publisher, by accepting the article for publication, acknowledges that the United States Government retains a non-exclusive, paid-up, irrevocable, world-wide license to publish or reproduce the published form of this manuscript, or allow others to do so, for United States Government purposes. A portion of this work was supported by the U.S. DOE NNSA. J.L.N. is appreciative to G. Granroth for assistance with the multiphonon package.

- [1] B. O. Loopstra, *J. Appl. Cryst.* **3**, 94 (1970).
- [2] H. Inaba, H. Shimizu, and K. Naito, *J. Nucl. Mat.* **64**, 66 (1977).
- [3] R. J. Ackermann, A. T. Chang, and C. A. Sorrell, *J. Inorg. Nucl. Chem.* **39**, 75 (1977).
- [4] F. Grønvd, *J. Inorg. Nucl. Chem.* **1**, 357 (1955).
- [5] W. Ermischer, O. Hauser, and M. Schenk, *J. Nucl. Mat.* **16**, 341 (1965).
- [6] S. Siegel, *Acta Cryst.* **8**, 617 (1955).
- [7] B. O. Loopstra, *Acta Cryst.* **B26**, 656 (1970).
- [8] R. Herak, *J. Inorg. Nucl. Chem.* **32**, 3793 (1970).
- [9] M. J. M. Leask, L. E. J. Roberts, A. J. Walter, and W. P. Wolf, *J. Chem. Soc.*, 4788 (1963).
- [10] E. F. Westrum and F. Grønvd, *J. Am. Chem. Soc.* **81**, 1777 (1959).
- [11] R. G. J. Ball and P. G. Dickens, *J. Mater. Chem.* **1**, 105 (1991).
- [12] H. He, D. A. Andersson, D. D. Allred, and K. D. Rector, *J. Phys. Chem. C* **117**, 16540 (2013).
- [13] Y. Yun, J. Ruzs, M. T. Suzuki, and P. M. Oppeneer, *Phys. Rev. B* **83**, 075109 (2011).
- [14] H. Y. Geng, H. X. Song, K. Jin, S. K. Xiang, and Q. Wu, *Phys. Rev. B* **84**, 174115 (2011).
- [15] X.-D. Wen, R. L. Martin, G. E. Scuseria, S. P. Rudin, E. R. Batista, and A. K. Burrell, *J. Phys.: Condens. Matter* **25**, 025501 (2013).
- [16] J. I. Ranasinghe, L. Malakkal, E. Jossou, B. Szpunar, and J. A. Szpunar, *Comp. Mat. Sci.* **171**, 109264 (2020).
- [17] N. A. Brincat, S. C. Parker, M. Molinari, G. C. Allen, and M. T. Storr, *Dalton Trans.* **44**, 2613 (2015).
- [18] A. Miskowiec, J. L. Niedziela, T. L. Spano, M. W. Ambrogio, S. Finkeldei, R. Hunt, and A. E. Shields, *J. Nucl. Mater.* **527**, 151790 (2019).
- [19] A. Miskowiec, T. Spano, R. Hunt, A. E. Shields, J. L. Niedziela, and S. Finkeldei, *Phys. Rev. Materials* **4**, 093610 (2020).
- [20] D. L. Abernathy, M. B. Stone, M. J. Loguillo, M. S. Lucas, O. Delaire, X. Tang, J. Y. Lin, and B. Fultz, *Rev. Sci. Instrum.* **83**, 015114 (2012).
- [21] M. B. Stone, J. L. Niedziela, M. J. Loguillo, M. A. Overbay, and D. L. Abernathy, *Rev. Sci. Instrum.* **85**, 085101 (2014).
- [22] M. B. Stone, J. L. Niedziela, D. L. Abernathy, L. DeBeer-Schmitt, G. Ehlers, O. Garlea, G. E. Granroth, M. Graves-Brook, A. I. Kolesnikov, A. Podlesnyak, and B. Winn, *Rev. Sci. Instrum.* **85**, 045113 (2014).
- [23] M. B. Stone, J. L. Niedziela, M. A. Overbay, and D. L. Abernathy, *EPJ Web Conf.* **83**, 03014 (2015).
- [24] F. C. Nix and D. McNair, *Phys. Rev.* **60**, 597 (1941).
- [25] O. Arnold, J. Bilheux, J. Borreguero, A. Buts, S. Campbell, L. Chapon, M. Doucet, N. Draper, R. F. Leal, M. Gigg, V. Lynch, A. Markvardsen, D. Mikkelsen, R. Mikkelsen, R. Miller, K. Palmen, P. Parker, G. Passos, T. Perring, P. Peterson, S. Ren, M. Reuter, A. Savici, J. Taylor, R. Taylor, R. Tolchenov, W. Zhou, and J. Zikovsky, *Nucl. Instrum. Meth. A* **764**, 156 (2014).
- [26] M. Kresch, O. Delaire, R. Stevens, J. Y. Y. Lin, and B. Fultz, *Phys. Rev. B* **75**, 104301 (2007).
- [27] J. Lin, F. Islam, and M. Kresh, *J. Open Source Softw.* **3**, 440 (2018).
- [28] G. L. Squires, *Introduction to the Theory of Thermal Neutron Scattering*, 3rd ed. (Cambridge University Press, Cambridge, 2009).
- [29] P. Brüesch, *Phonons: Theory and Experiments I*, Springer Series in Solid-State Sciences, Vol. 34 (Springer Berlin, Heidelberg, 1982).
- [30] D. L. Abernathy, J. L. Niedziela, and M. B. Stone, *EPJ Web Conf.* **83**, 03001 (2015).
- [31] J. P. Allen and G. W. Watson, *Phys. Chem. Chem. Phys.* **16**, 21016 (2014).
- [32] J. P. Perdew, A. Ruzsinszky, G. I. Csonka, O. A. Vydrov, G. E. Scuseria, L. A. Constantin, X. Zhou, and K. Burke, *Phys. Rev. Lett.* **100**, 136406 (2008).
- [33] P. E. Blöchl, O. Jepsen, and O. K. Andersen, *Phys. Rev. B* **49**, 16223 (1994).
- [34] S. L. Dudarev, G. A. Botton, S. Y. Savrasov, C. J. Humphreys, and A. P. Sutton, *Phys. Rev. B* **57**, 1505 (1998).
- [35] G. Beridze and P. M. Kowalski, *J. Phys. Chem. A* **118**, 11797 (2014).
- [36] M. Cococcioni and S. de Gironcoli, *Phys. Rev. B* **71**, 035105 (2005).
- [37] A. Togo and I. Tanaka, *Scr. Mater.* **108**, 1 (2015).
- [38] A. Togo, L. Chaput, and I. Tanaka, *Phys. Rev. B* **91**, 094306 (2015).
- [39] B. Fultz, *Prog. Mater. Sci.* **55**, 247 (2010).
- [40] J. M. Lawrence, P. S. Riseborough, and R. D. Parks, *Rep. Prog. Phys.* **44**, 1 (1981).
- [41] P. A. Alekseev, J.-M. Mignot, E. V. Nefedova, K. S. Nemkovski, V. N. Lazukov, N. N. Tiden, A. P. Menushenkov, R. V. Chernikov, K. V. Klementiev, A. Ochiai, A. V. Golubkov, R. I. Bewley, A. V. Rybina, and I. P. Sadikov, *Phys. Rev. B* **74**, 035114 (2006).
- [42] B. H. Grier, S. M. Shapiro, C. F. Majkrzak, and R. D. Parks, *Phys. Rev. Lett.* **45**, 666 (1980).
- [43] B. H. Grier, R. D. Parks, S. M. Shapiro, and C. F. Majkrzak, *Phys. Rev. B* **24**, 6242 (1981).
- [44] C.-K. Loong, B. H. Grier, S. M. Shapiro, J. M. Lawrence, R. D. Parks, and S. K. Sinha, *Phys. Rev. B* **35**, 3092 (1987).
- [45] D. Wallace, *Thermodynamics of Crystals* (Dover Publications, Mineola, New York, 1972).
- [46] <http://energy.gov/downloads/doe-public-access-plan>.